

Rutile IrO₂/TiO₂ superlattices: A hyperconnected analog to the Ruddelsden-Popper structureJason K. Kawasaki,^{1,2,3} David Baek,⁴ Hanjong Paik,⁵ Hari P. Nair,⁶ Lena F. Kourkoutis,⁴
Darrell G. Schlom,^{1,6} and Kyle M. Shen^{1,2}¹*Kavli Institute at Cornell for Nanoscale Science, Cornell University, Ithaca, New York 14853, USA*²*Laboratory for Atomic and Solid State Physics, Cornell University, Ithaca, New York 14853, USA*³*Department of Materials Science and Engineering, University of Wisconsin, Madison, Wisconsin 53706, USA*⁴*Applied Physics, Cornell University, Ithaca, New York 14853, USA*⁵*Platform for the Accelerated Realization, Analysis, & Discovery of Interface Materials (PARADIM), Cornell University, Ithaca, New York 14853, USA*⁶*Department of Materials Science and Engineering, Cornell University, Ithaca, New York 14853, USA*

(Received 3 April 2018; revised manuscript received 3 May 2018; published 23 May 2018)

Dimensionality and connectivity among octahedra play important roles in determining the properties, electronic structure, and phase transitions of transition-metal oxides. Here we demonstrate the epitaxial growth of (110)-oriented alternating layers of IrO₂ and TiO₂, both of which have the rutile structure. These (IrO₂)_n/(TiO₂)₂ superlattices consist of IrO₆ and TiO₆ octahedra tiled in a hyperconnected, edge- and corner-sharing network. Despite the large lattice mismatch between constituent layers ($\Delta d_{\parallel} = -2.1\%$ and $\Delta c = +6.6\%$), our reactive molecular-beam epitaxy-grown superlattices show high structural quality as determined by x-ray diffraction and sharp interfaces as observed by transmission electron microscopy. The large strain at the interface is accommodated by an ordered interfacial reconstruction. The superlattices show persistent metallicity down to $n = 3$ atomic layers, and angle-resolved photoemission spectroscopy measurements reveal quantized sub-bands with signatures of IrO₂-IrO₂ interlayer coupling.

DOI: [10.1103/PhysRevMaterials.2.054206](https://doi.org/10.1103/PhysRevMaterials.2.054206)

Transition-metal oxide superlattices enable the discovery of emergent properties at interfaces and precise manipulation of magnetic [1], electronic [2,3], and ferroic properties [4,5]. To date, efforts have focused primarily on superlattices in the perovskite ($AMO_3/A'M'O_3$) [1,4–6] and related naturally layered Ruddelsden-Popper ($A_{n+1}M_nO_{3n+1}$) [7–10] structures, which consist of MO_6 octahedra tiled in all corner-sharing networks. In such superlattices the primary tuning knobs are the chemistry of the transition-metal cations M (M'), the layer thickness, and epitaxial strain.

More drastic property changes can, however, be made by altering the connectivity (topology) of the MO_6 octahedral network. The rutile polymorph (composition MO_2) is one such example, which consists of a mixed edge- and corner-sharing network (Fig. 1). This hyperconnectivity enhances direct M - M interactions along the $[001]_r$ edge-sharing direction (r denotes the conventional rutile unit cell), in contrast with the primarily oxygen-mediated M - O - M interactions in corner-sharing perovskites and Ruddelsden-Popper structures, and is a key driver in determining the relationships between structure and electronic properties in these materials. For example, the metal-insulator transition in VO₂ is driven by direct V-V dimerization in a Mott-Peierls-like mechanism [11–13]. The strength of M - M interactions and octahedral connectivity can also tune the effective strength of electron-electron correlations [14]. Finally, the rutile structure belongs to a nonsymmorphic space group, an important symmetry for stabilizing topological states and the spin Hall effect [15–18]. Together, these factors point to octahedral connectivity as a potentially new and important tuning parameter for controlling oxide superlattices.

Unfortunately, the combination of large lattice mismatches between different MO_2 compounds and high surface energies has made the growth of all-rutile superlattices challenging [19,20].

Here we demonstrate the epitaxial growth and characterization of the atomic and electronic structure of all-rutile IrO₂/TiO₂ superlattices. The $(110)_r$, where the r subscript refers to the conventional unit cell of the rutile polymorph, was chosen for the plane of the surface due to its low surface energy to facilitate smooth growth, as opposed to the high surface energy $(001)_r$ orientation [21]. We choose IrO₂ as the electronically active layer due to the delicate interplay of spin-orbit coupling and electron-electron correlations in the iridates, which lead to spin-orbit Mott physics [22], proposed topological states [8,23], and possible novel superconductivity in the two-dimensional limit [24–26]. More specifically, rutile IrO₂ exhibits a large spin Hall effect [27] and unusual transport properties in which the sign of the apparent carrier can be tuned via the orientation of the magnetic field [28].

In the rutile polymorph of IrO₂, the Ir⁴⁺ cations have an electron configuration of $5d^5$, the same as its perovskite and Ruddelsden-Popper cousins SrIrO₃ and Sr _{$n+1$} Ir _{n} O _{$3n+1$} . The rutile TiO₂, which has configuration $3d^0$, was chosen as the insulating barrier layer due to its large band gap. Hence, our all-rutile IrO₂/TiO₂ ($5d^5/3d^0$) superlattices can be viewed as a hyperconnected analog of (SrIrO₃) _{n} /(SrTiO₃) _{m} perovskite and Sr _{$n+1$} Ir _{n} O _{$3n+1$} Ruddelsden-Popper superlattices. The latter two have exhibited metal-insulator transitions and the onset of magnetic ordering near $n = 3$ perovskite layers [6,9]. Similarly, recent first-principles calculations for (001) -

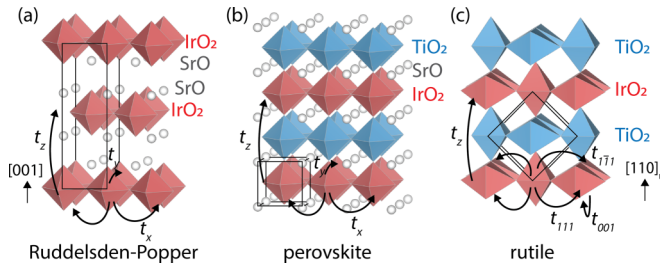


FIG. 1. Comparison between (001)-oriented Ruddelsden-Popper and perovskite superlattices, with (110)-oriented rutile superlattices. Transition-metal cations M are located at the center of each octahedra, and oxygen is at the corners. Both Ruddelsden-Popper and perovskite superlattices are characterized by four oxygen-mediated $M-O-M$ nearest neighbor hoppings in the (001) plane (arrows). In contrast, the rutile structure is characterized by chains of edge-sharing octahedra oriented along $[001]_r$ (into the page). In the (110) plane it has four $M-O-M$ hoppings, plus direct $M-M$ hopping along $[001]_r$.

$(\text{IrO}_2)_n/(\text{TiO}_2)_2$ superlattices with periodicity $n = 3, 4,$ and 5 atomic layers were grown by reactive oxide molecular-beam epitaxy (MBE) on HF-etched (110)-oriented rutile TiO_2 substrates. Growth was performed at 350°C as calibrated by a pyrometer, using a background partial pressure of 10^{-6} Torr of distilled ozone as the oxidant. The superlattice structure was defined by alternating shutter-controlled doses of Ir and Ti, each containing the number of atoms in a single monolayer of IrO_2 or TiO_2 . These fluxes were supplied from an electron beam evaporator and a Ti ball, respectively [14]. Film growth was characterized in real time by reflection high-energy electron diffraction (RHEED). After growth, samples were transferred through an ultrahigh vacuum manifold ($p < 3 \times 10^{-10}$ Torr) and characterized by *in situ* low-energy electron diffraction (LEED), and *in situ* angle-resolved photoemission spectroscopy (ARPES) at 20 K using the $I\alpha$ emission line from a monochromated He lamp ($h\nu = 21.2$ eV) and Scienta R4000 analyzer. Samples were also characterized *ex situ* by high-resolution x-ray diffraction (XRD, with $\text{Cu K}\alpha$ radiation), magnetotransport (Quantum Design PPMS), and scanning transmission electron microscopy (STEM).

oriented rutile $\text{IrO}_2/\text{TiO}_2$ superlattices suggest metal-insulator transitions and magnetic ordering near $n = 2-3$ [29].

The shutter timing and RHEED response of our growth method is illustrated in Fig. 2. During growth we observe

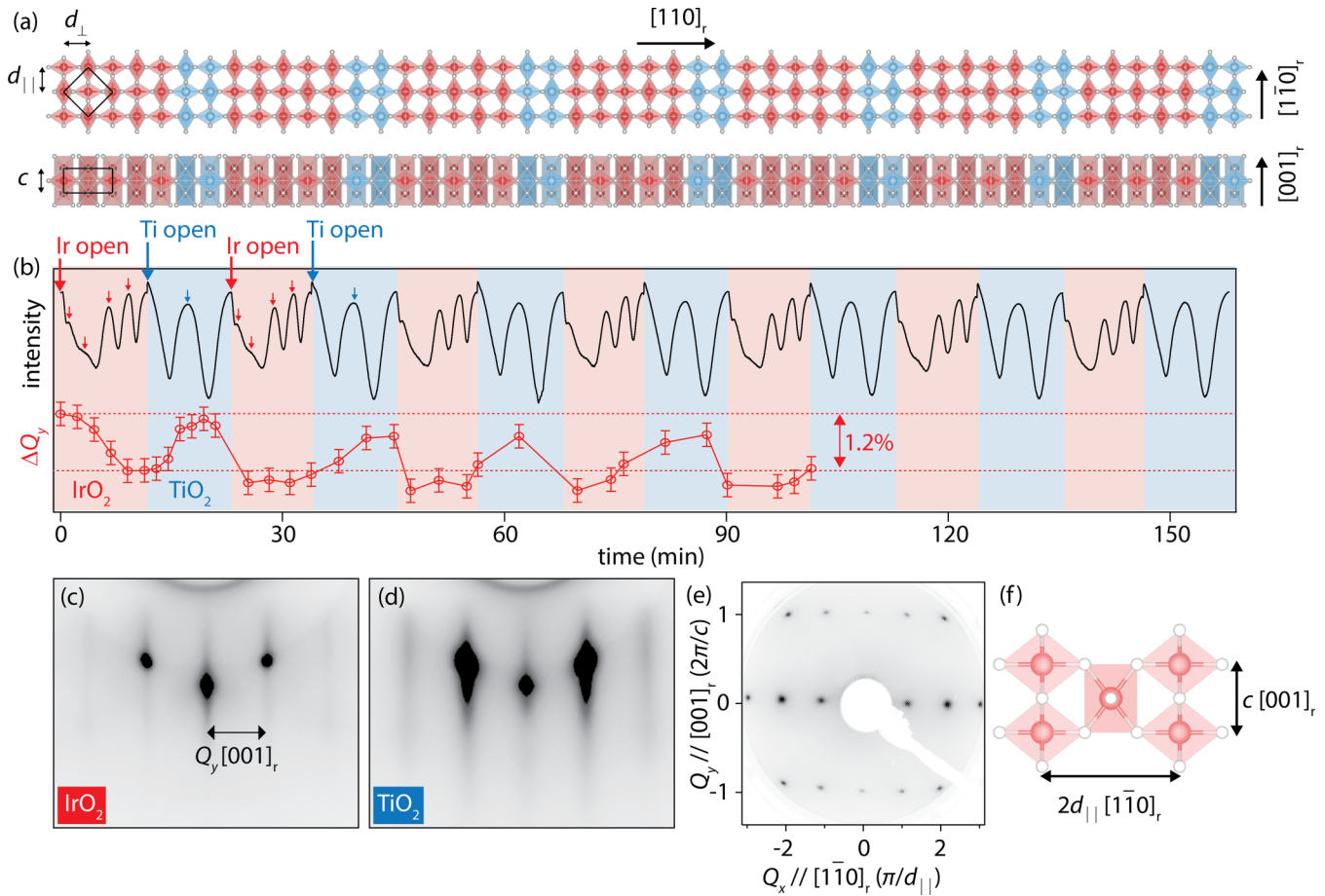


FIG. 2. Growth of $(\text{IrO}_2)_n/(\text{TiO}_2)_2$ superlattices. (a) Crystal structure of an $n = 5$ superlattice. We define $d_\perp \parallel [110]_r$, as the average out-of-plane atomic spacing, and $d_\parallel \parallel [1\bar{1}0]_r$ and $c \parallel [001]_r$, as the in-plane spacings. (b) RHEED intensity oscillations of the (0, 1) spot (top black curve). The bottom red curve shows modulations of the in-plane c lattice spacing ($Q_y \parallel c$), as extracted from horizontal line cuts of the RHEED pattern. (c), (d) RHEED patterns for IrO_2 and TiO_2 along the $[1\bar{1}0]_r$ azimuth. (e) LEED pattern of an IrO_2 -terminated superlattice at 100 eV. (f) In-plane crystal structure the top layer of IrO_2 as viewed down the $[110]_r$ direction.

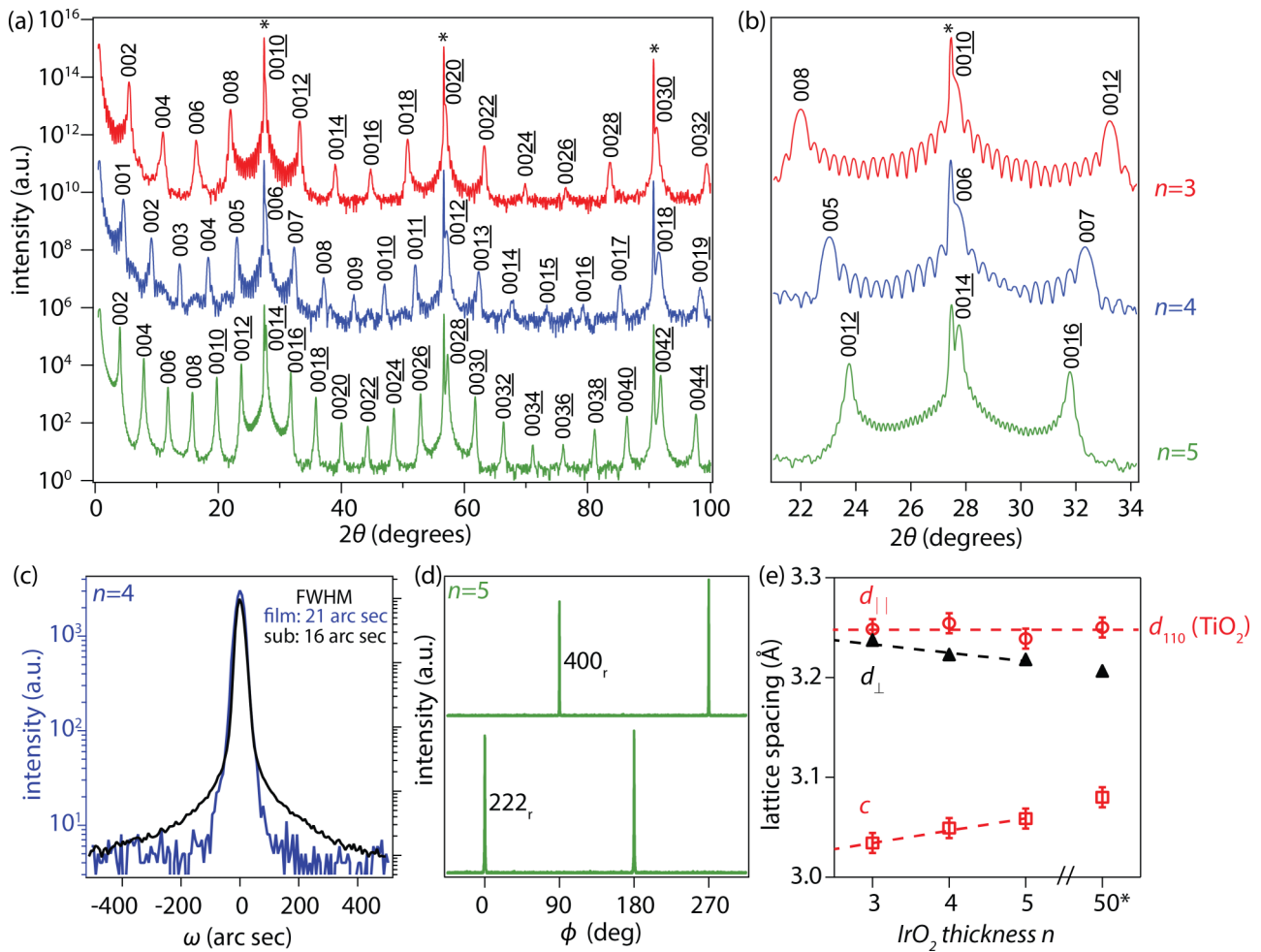


FIG. 3. X-ray diffraction for $(\text{IrO}_2)_n/(\text{TiO}_2)_2$ superlattices with $n = 3, 4,$ and 5 (16, 12, and 24 repeat units, respectively). (a) Wide angle θ - 2θ scan showing well resolved superlattice peaks up to high angle. (b) Finer θ - 2θ scan around the 110_r substrate reflection, showing superlattice peaks and Kiessig fringes. Film reflections are indexed to the superlattice coordinate system, where $[001]_{SL} \parallel [110]_r$. Substrate reflections are marked by asterisks “*”. (c) Rocking curves of the 005_{SL} reflection of the $n = 4$ superlattice, compared to the 110 reflection of the TiO_2 substrate. (d) In-plane rotation ϕ scans of the film showing the epitaxial alignment. $\phi = 0^\circ$ corresponds to the in-plane component of the diffraction vector aligned parallel to the $[001]$ direction of the TiO_2 substrate. (e) In-plane (red, $d_{\parallel} \parallel [1\bar{1}0]_r$, $c \parallel [001]_r$) and average out-of-plane (black, $d_{\perp} \parallel [110]_r$) lattice spacings. For all films, the in-plane d_{\parallel} remains commensurate with that of the TiO_2 substrate.

clear periodic modulations in the RHEED intensity [Fig. 2(b)], where each oscillation corresponds to one IrO_2 (TiO_2) monolayer (ML). The oscillation periods are in good agreement with flux measurements by a quartz crystal microbalance (QCM) and XRD Kiessig fringes on calibration samples. The corresponding RHEED patterns for the IrO_2 and TiO_2 are characterized by a sharp arc of spots [Figs. 2(c) and 2(d)], indicating smooth epitaxial growth. The epitaxial alignment is further confirmed by the sharp spots in the final LEED pattern [Fig. 2(e)].

During the first two monolayers of IrO_2 growth on TiO_2 , we observe a decaying envelope in the RHEED intensity, with the oscillation amplitude recovering in the third and subsequent layers. Interestingly there is no such decaying envelope for the opposite growth sequence, TiO_2 on IrO_2 . We interpret this asymmetry to result from differences in wetting: first-principles calculations suggest that the (110) surface energy for TiO_2 (0.9 J/m^2 [21]) is smaller than that of IrO_2 (1.4 J/m^2 [30]) implying a greater tendency for TiO_2 to wet IrO_2 than vice versa.

We also observe periodic modulations of the in-plane $c \parallel [001]_r$ lattice spacing during growth, for which there is a large mismatch of 6.6%. The red curve in Fig. 2(b) plots the changes in c at the surface, as extracted from Gaussian fitted horizontal line cuts of the RHEED intensity [Figs. 2(c) and 2(d)]. We find that c expands (Q_y decreases) during growth of IrO_2 and contracts (Q_y increases) during growth of TiO_2 . The magnitude of change from layer to layer is 1.2% and there is also an envelope of increasing c as the growth persists, indicating partial relaxation along the c axis. Along the other in-plane direction, $[1\bar{1}0]_r$ (d_{\parallel}), for which the mismatch is smaller (-2.1%), we do not observe changes in the Q spacing within a resolution of $\Delta Q/Q \approx 0.3\%$, indicating that d_{\parallel} remains commensurate to the substrate.

The resulting superlattices show high structural quality as measured by x-ray diffraction. This is quite remarkable given the large mismatch between the IrO_2 and TiO_2 constituent layers ($\Delta d_{\parallel} = -2.1\%$ and $\Delta c = +6.6\%$). Figures 3(a) and 3(b) show symmetric θ - 2θ scans for $n = 3, 4,$ and 5 superlattices (16, 12, and 24 repeat units, respectively). We observe all

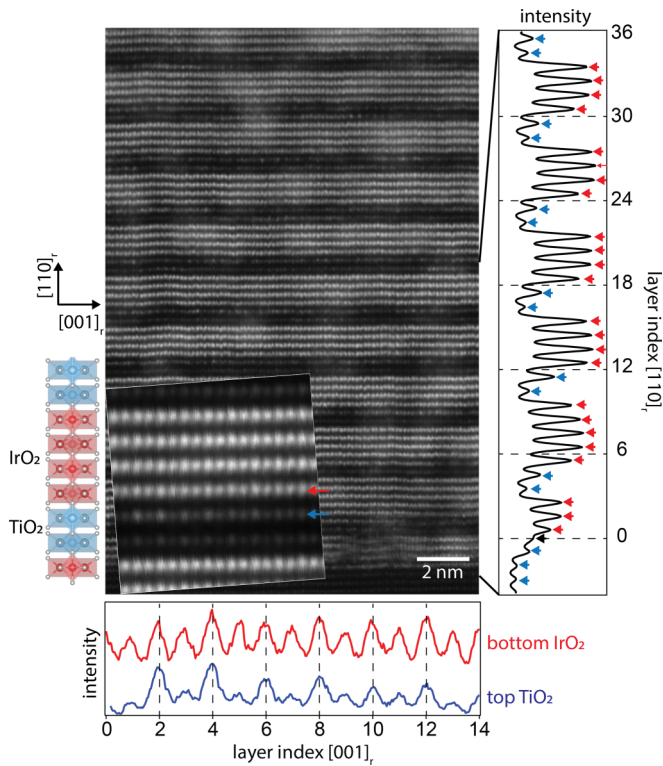


FIG. 4. ADF-STEM image of the $n = 4$ superlattice, with corresponding intensity line cuts. The vertical line cut along the $[110]_r$ growth direction is averaged over the entire frame. The horizontal line cut along $[001]_r$ is localized to the bottom IrO_2 atomic layer (red) and the top TiO_2 atomic layer (blue). The inset shows a $2\times$ intensity modulation at the top TiO_2 layer of the TiO_2 -on- IrO_2 interface.

of the expected superlattice reflections out to $2\theta = 100^\circ$ as well as Kiessig finite thickness fringes indicating sharp interfaces [Figs. 3(a) and 3(b)]. Rocking curves are similarly sharp, with full width at half maxima (FWHM) of 23, 21, and 28 arc sec for the $n = 3, 4,$ and 5 samples, respectively, comparable to the substrate, indicating high structural quality despite the large lattice mismatch between IrO_2 and TiO_2 . These rocking curve widths are comparable to MBE-grown perovskite and Ruddelsden-Popper superlattices [31]. The in-plane epitaxial alignment to TiO_2 (110) is confirmed by ϕ scans of the film 222_r and 400_r reflections, which show twofold rotation and no in-plane rotation twin variants.

In Fig. 3(e) we plot the measured in-plane (red) and average out-of-plane (black) lattice spacings for the $n = 3, 4,$ and 5 superlattices and for a 50 monolayer thick IrO_2 film. The average out-of-plane spacing d_\perp , determined from Nelson-Riley extrapolations of the on-axis 2θ scans, decreases with monotonically with n as expected from Vegard's law. The in-plane lattice spacings d_\parallel and c were extracted from projections of the off-axis 400_r and 222_r reflections, respectively. We find that while d_\parallel remains commensurate to the substrate, c partially relaxes. Both trends in c and d_\parallel are in agreement with the lattice parameters extracted from RHEED [Fig. 2(b)].

To further explore the interface structure and partial relaxation we perform cross-sectional annular dark field (ADF) STEM measurements of the $n = 4$ sample (Fig. 4). Here, due to the higher atomic mass of Ir, columns of Ir atoms appear

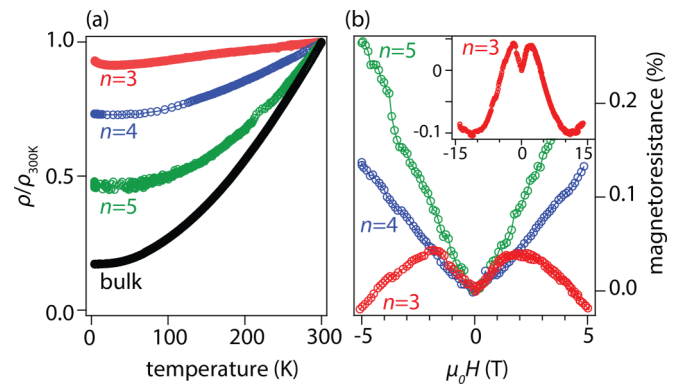


FIG. 5. (a) Zero field resistivity for the $n = 3, 4,$ and 5 superlattices and for a 50 monolayer (bulklike) IrO_2 film. (b) Longitudinal magnetoresistance with perpendicular magnetic field, measured at 2K.

as bright regions while columns of Ti appear as the darker regions. The frame averaged line cut along the $[110]_r$ growth direction confirms the stacking sequence of four monolayers of IrO_2 and two monolayers of TiO_2 .

Higher-resolution imaging of the IrO_2 on TiO_2 interface (insert) and layer-resolved horizontal line cuts (bottom) reveal a periodic modulation of the STEM intensity in the topmost TiO_2 layer (blue curve), with periodicity twice that of the atomic $[001]_r$ spacing. No obvious superstructure appears in the bottom-most IrO_2 layer (red curve). We interpret this modulation to result from an interfacial reconstruction that partially relieves stresses at the $\text{IrO}_2/\text{TiO}_2$ interface due to the large lattice mismatch. Such a reconstruction may explain why well-defined $\text{IrO}_2/\text{TiO}_2$ superlattices are able to form, despite the mismatch. This interfacial reconstruction may also be responsible for the decay in the RHEED intensity during the initial growth of IrO_2 on TiO_2 [Fig. 2(b)].

Temperature-dependent transport measurements reveal that all superlattices remain metallic ($\partial\rho/\partial T > 0$) [Fig. 5(a)] down to $n = 3$ layers. For the $n = 4$ and $n = 5$ superlattices, the zero-field resistivity follows a temperature squared dependence from 2–300 K, consistent with Fermi liquid behavior. For $n = 3$ there is a small upturn in the low-temperature resistivity, which we attribute to weak antilocalization in the two-dimensional limit, but the overall temperature dependence indicates metallic behavior.

The retained metallicity of our rutile superlattices is quite notable, as in purely corner-sharing $(\text{SrIrO}_3)_n/(\text{SrTiO}_3)_1$ perovskite superlattices, the $n = 3$ member is insulating [6]. For $\text{Sr}_{n+1}\text{Ir}_n\text{O}_{3n+1}$ Ruddelsden-Popper superlattices, a metal-insulator transition is expected in the vicinity of $n = 2-3$ atomic layers [8,9]. The retained metallicity for our rutile superlattices results from the higher degree of octahedral connectivity and wider bandwidths in the rutile structure, as discussed in recent ARPES studies of IrO_2 [14].

Magnetoresistance measurements at 2 K confirm the weak antilocalization [Fig. 5(b), insert], as evidenced by a narrow local minimum in the magnetoresistance superimposed on a broader maximum at zero field. Fitting to a Hikami-Larkin-Nagaoka model [32] we extract a magnetic dephasing length of approximately 100 nm. For the thicker $n = 4$ and five

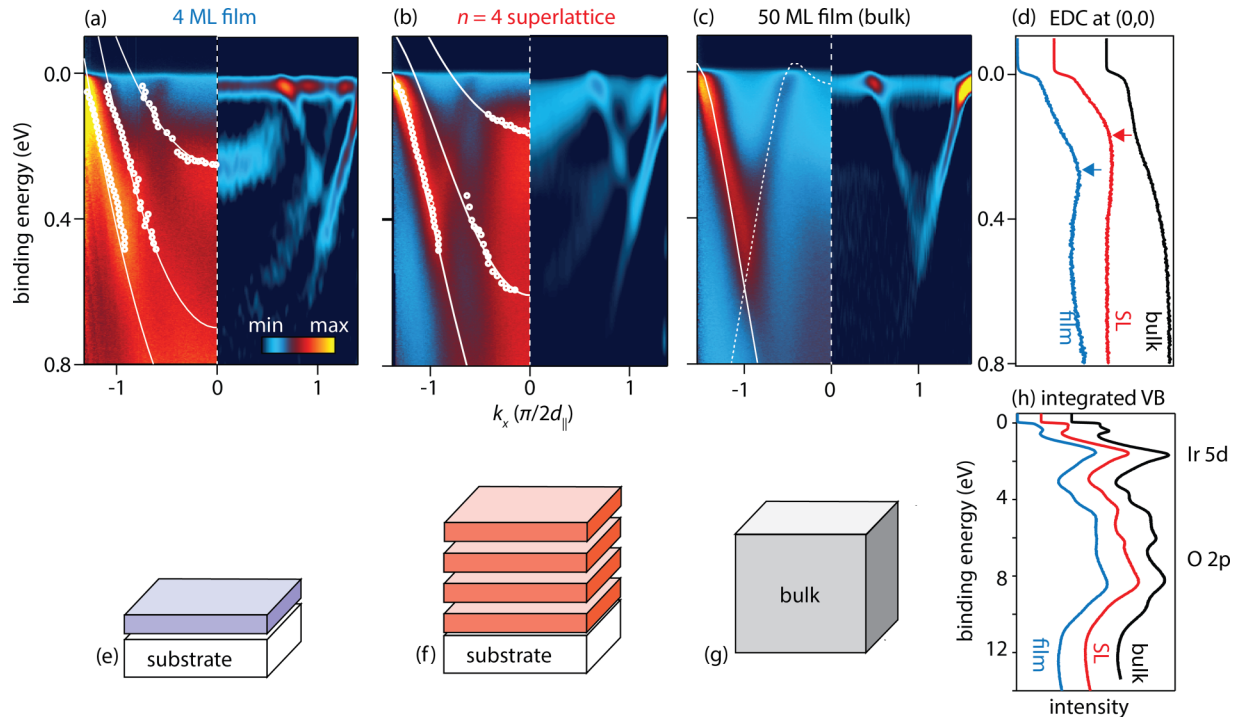


FIG. 6. ARPES measurements of (a) a 4 ML ultrathin IrO₂ film, (b) the $n = 4$ superlattice (IrO₂-terminated, $[(\text{IrO}_2)_4/(\text{TiO}_2)_2] \times 12$), and (c) a bulklike 50 ML thick film, using He I α photons ($h\nu = 21.2$ eV). The dispersion is through the zone center (0,0), $k_x \parallel [1\bar{1}0]$. All samples were grown on TiO₂ (110). The left-hand side shows the raw photoemission intensity (color scale) and peak positions from fitting of the energy and momentum distribution curves (EDC/MDC, circles). The right-hand side shows the second derivative of the intensity $-\partial^2 I/\partial E^2$. Solid curves in (a) and (b) are guides to the eye, curves in (c) are the calculated dispersion from density functional theory, using the generalized gradient approximation and including spin-orbit coupling (GGA+SO) [14]. (d) Energy dispersion curve (EDC) at $k_{\parallel} = (0,0)$, showing a shift in the quantum well binding energies (arrows) and energy broadening for the superlattice. (e)–(g) Cartoon structures for the ultrathin film, superlattice, and bulklike samples. (h) Angle integrated measurements of the valence bands using He II α photons ($h\nu = 40.8$ eV).

superlattices we observe a linear dependence of the magnetoresistance on field, consistent with a low-density semimetal.

ARPES measurements on the superlattices reveal quantized sub-bands with signatures of interlayer IrO₂-IrO₂ coupling. In Fig. 6 we compare measurements for an $n = 4$ superlattice (IrO₂-terminated, $[(\text{IrO}_2)_4/(\text{TiO}_2)_2] \times 12$), with that of a 4 ML ultrathin IrO₂ film and a bulklike, 50 ML thick IrO₂ film. All three structures are characterized by a broad band of oxygen 2p states from binding energies of 10–3 eV, and a band of iridium 5d states extending from 3 eV to the Fermi energy [Fig. 6(h)], in agreement with previous ARPES and density functional theory studies of bulk IrO₂ [14]. Zooming in to the Fermi level [Figs. 6(a)–6(c)], the bulklike sample is characterized by two highly dispersive bands (bandwidth greater than 1.5 eV) that are well described by density functional theory calculations (solid curves) [14]. For the 4 ML thin film, we observe additional electronlike bands that we attribute to metallic quantum well states, resulting from strong spatial confinement in the out-of-plane direction [33], which cross through the Fermi energy. These sub-bands are highly reminiscent of the sharp quantum well sub-bands observed in ultrathin films of SrVO₃ with perovskite structure [34]. We emphasize two important differences between our IrO₂/TiO₂ superlattices and the SrVO₃ ultrathin films: (i) our IrO₂/TiO₂ crystallize in the rutile structure as opposed to the perovskite structure of SrVO₃, and (ii) our IrO₂/TiO₂ samples are in superlattice form with a finite number of repeats, as opposed to a singly layered SrVO₃

thin film, and are thus expected to be more robust to external perturbations such as surface contamination.

Comparing the 4 ML ultrathin film to the $n = 4$ superlattice, we also observe three occupied sub-bands; however, the sub-bands in the superlattice differ from that of the ultrathin film in two respects: (i) their binding energies are shallower (shifted upwards in energy towards the Fermi energy by ~ 100 meV) and (ii) they are broadened in energy, as shown in the energy dispersion curves [EDCs, Fig. 6(d)]. We interpret these differences to arise from IrO₂-IrO₂ interlayer coupling, in which tunneling across the TiO₂ barriers causes the quantized states residing within each IrO₂ quantum well to hybridize with states in neighboring quantum wells, resulting in a finite out-of-plane dispersion. The TiO₂ barrier thickness provides a degree of freedom for tuning the electronic structure and the effective k_z dispersion of the superlattice sub-bands, which does not exist for an ultrathin film. The sharpness of the barrier, i.e., the sharpness of the IrO₂/TiO₂ interfaces, as well its structure, e.g. an ordered interfacial reconstruction, are expected to be additional parameters for tuning the sub-band dispersions. The full thickness-dependent evolution of the quantum well states for ultrathin films is the subject of a concurrent publication [33]. In addition to the quantum well states, in some samples we also observe subtle kinks in the dispersion at characteristic energy of approximately 80 meV, comparable to the Debye temperature of IrO₂ (700 K ≈ 60 meV [35]). Therefore we speculate the kink may arise from electron-phonon coupling.

In summary, we have demonstrated the epitaxial growth of all-rutile $\text{IrO}_2/\text{TiO}_2$ $(110)_r$ superlattices by reactive oxide MBE. This layered rutile structure can be viewed as a hyper-connected, nonsymmorphic alternative to the perovskite and Ruddlesden-Popper oxide structures that are more commonly studied. Our superlattices show high structural quality as determined by x-ray diffraction, with all of the expected superlattice reflections out to $2\theta = 100^\circ$, and rocking curve widths comparable to the best perovskite and Ruddlesden-Popper superlattices. This is quite remarkable given the large mismatch between the IrO_2 and TiO_2 constituent layers ($\Delta d_{\parallel} = -2.1\%$ and $\Delta c = +6.6\%$). Cross-sectional transmission electron microscopy suggests that the large strain is accommodated by an interfacial reconstruction. The higher octahedral connectivity in the rutile structure provides a greater tendency toward retained metallicity, as compared to the insulating behavior in perovskite and Ruddlesden-Popper iridate superlattices. ARPES measurements reveal quantum confined, metallic subbands with interlayer coupling. Due to the highly anisotropic crystal structure of rutile, with chains of edge-sharing octahedra oriented along $[001]_r$, we expect the electronic properties of rutile superlattices to be highly dependent on orientation.

For example, while our $(110)_r$ -oriented superlattices exhibit retained metallicity, $(001)_r$ -oriented superlattices appear to be more likely to yield metal-insulator transitions, as interfaces in this orientation break the continuity of edge-sharing IrO_6 chains [29]. Realizing high-quality superlattices in the high surface energy $(001)_r$ orientation, however, remains an outstanding challenge [19,20]. This interplay of anisotropy, topology, octahedral connectivity, and reduced dimensionality in the rutile structure presents a new platform for tuning the properties of oxide superlattices.

This work was supported by the National Science Foundation [Platform for the Accelerated Realization, Analysis, and Discovery of Interface Materials (PARADIM)] under Cooperative Agreement No. DMR-1539918. This work made use of the Cornell Center for Materials Research (CCMR) Shared Facilities, which are supported through the NSF MRSEC program (DMR-1120296). Substrate preparation was performed in part at the Cornell NanoScale Facility, a member of the National Nanotechnology Coordinated Infrastructure (NNCI), which is supported by the NSF (Grant No. ECCS-1542081).

-
- [1] H. Yamada, Y. Ogawa, Y. Ishii, H. Sato, M. Kawasaki, H. Akoh, and Y. Tokura, Engineered interface of magnetic oxides, *Science* **305**, 646 (2004).
- [2] A. Ohtomo and H. Y. Hwang, A high-mobility electron gas at the $\text{LaAlO}_3/\text{SrTiO}_3$ heterointerface, *Nature (London)* **427**, 423 (2004).
- [3] N. Reyren, S. Thiel, A. D. Caviglia, L. F. Kourkoutis, G. Hammerl, C. Richter, C. W. Schneider, T. Kopp, A.-S. Rüetschi, D. Jaccard *et al.*, Superconducting interfaces between insulating oxides, *Science* **317**, 1196 (2007).
- [4] A. S. Disa, D. P. Kumah, A. Malashevich, H. Chen, D. A. Arena, E. D. Specht, S. Ismail-Beigi, F. J. Walker, and C. H. Ahn, Orbital Engineering in Symmetry-Breaking Polar Heterostructures, *Phys. Rev. Lett.* **114**, 026801 (2015).
- [5] H. N. Lee, H. M. Christen, M. F. Chisholm, C. M. Rouleau, and D. H. Lowndes, Strong polarization enhancement in asymmetric three-component ferroelectric superlattices, *Nature* **433**, 395 (2005).
- [6] J. Matsuno, K. Ihara, S. Yamamura, H. Wadati, K. Ishii, V. V. Shankar, Hae-Young Kee, and H. Takagi, Engineering a Spin-Orbital Magnetic Insulator by Tailoring Superlattices, *Phys. Rev. Lett.* **114**, 247209 (2015).
- [7] J. H. Haeni, C. D. Theis, D. G. Schlom, W. Tian, X. Q. Pan, H. Chang, I. Takeuchi, and X.-D. Xiang, Epitaxial growth of the first five members of the $\text{Sr}_{n+1}\text{Ti}_n\text{O}_{3n+1}$ Ruddlesden-Popper homologous series, *Appl. Phys. Lett.* **78**, 3292 (2001).
- [8] J.-M. Carter, V. V. Shankar, M. A. Zeb, and H.-Y. Kee, Semimetal and topological insulator in perovskite iridates, *Phys. Rev. B* **85**, 115105 (2012).
- [9] A. Yamasaki, H. Fujiwara, S. Tachibana, D. Iwasaki, Y. Higashino, C. Yoshimi, K. Nakagawa, Y. Nakatani, K. Yamagami, H. Aratani, O. Kirilmaz, M. Sing, R. Claessen, H. Watanabe, T. Shirakawa, S. Yunoki, A. Naitoh, K. Takase, J. Matsuno, H. Takagi, A. Sekiyama, and Y. Saitoh, Three-dimensional electronic structures and the metal-insulator transition in Ruddlesden-Popper iridates, *Phys. Rev. B* **94**, 115103 (2016).
- [10] I. I. Mazin and D. J. Singh, Competitions in Layered Ruthenates: Ferromagnetism Versus Antiferromagnetism and Triplet Versus Singlet Pairing, *Phys. Rev. Lett.* **82**, 4324 (1999).
- [11] R. M. Wentzcovitch, W. W. Schulz, and P. B. Allen, VO_2 , *Phys. Rev. Lett.* **72**, 3389 (1994).
- [12] M. W. Haverkort, Z. Hu, A. Tanaka, W. Reichelt, S. V. Streltsov, M. A. Korotin, V. I. Anisimov, H. H. Hsieh, H.-J. Lin, C. T. Chen, D. I. Khomskii, and L. H. Tjeng, Orbital-Assisted Metal-Insulator Transition in VO_2 , *Phys. Rev. Lett.* **95**, 196404 (2005).
- [13] M. M. Qazilbash, M. Brehm, B.-G. Chae, P.-C. Ho, G. O. Andreev, B.-J. Kim, Sun Jin Yun, A. V. Balatsky, M. B. Maple, F. Keilmann *et al.*, Mott transition in VO_2 revealed by infrared spectroscopy and nano-imaging, *Science* **318**, 1750 (2007).
- [14] J. K. Kawasaki, M. Uchida, H. Paik, D. G. Schlom, and K. M. Shen, Evolution of electronic correlations across the rutile, perovskite, and Ruddlesden-Popper iridates with octahedral connectivity, *Phys. Rev. B* **94**, 121104 (2016).
- [15] L. Michel and J. Zak, Connectivity of energy bands in crystals, *Phys. Rev. B* **59**, 5998 (1999).
- [16] S. M. Young and C. L. Kane, Dirac Semimetals in Two Dimensions, *Phys. Rev. Lett.* **115**, 126803 (2015).
- [17] Yan Sun, Yang Zhang, Chao-Xing Liu, Claudia Felser, and Binghai Yan, Dirac nodal lines and induced spin hall effect in metallic rutile oxides, *Phys. Rev. B* **95**, 235104 (2017).
- [18] V. Pardo and W. E. Pickett, Half-Metallic Semi-Dirac-Point Generated by Quantum Confinement in TiO_2/VO_2 Nanostructures, *Phys. Rev. Lett.* **102**, 166803 (2009).
- [19] K. Shibuya, M. Kawasaki, and Y. Tokura, Metal-insulator transitions in TiO_2/VO_2 superlattices, *Phys. Rev. B* **82**, 205118 (2010).
- [20] C. A. Ramos, D. Lederman, A. R. King, and V. Jaccarino, New Antiferromagnetic Insulator Superlattices: Structural and

- Magnetic Characterization of (FeF₂)_m(CoF₂)_n, *Phys. Rev. Lett.* **65**, 2913 (1990).
- [21] M. Ramamoorthy, D. Vanderbilt, and R. D. King-Smith, First-principles calculations of the energetics of stoichiometric TiO₂ surfaces, *Phys. Rev. B* **49**, 16721 (1994).
- [22] B. J. Kim, H. Jin, S. J. Moon, J.-Y. Kim, B.-G. Park, C. S. Leem, J. Yu, T. W. Noh, C. Kim, S.-J. Oh, J.-H. Park, V. Durairaj, G. Cao, and E. Rotenberg, Novel $J_{\text{eff}} = 1/2$ Mott State Induced by Relativistic Spin-Orbit Coupling in Sr₂IrO₄, *Phys. Rev. Lett.* **101**, 076402 (2008).
- [23] Y. Chen and H.-Y. Kee, Topological phases in iridium oxide superlattices: Quantized anomalous charge or valley hall insulators, *Phys. Rev. B* **90**, 195145 (2014).
- [24] F. Wang and T. Senthil, Twisted Hubbard Model for Sr₂IrO₄: Magnetism and Possible High Temperature Superconductivity, *Phys. Rev. Lett.* **106**, 136402 (2011).
- [25] Y. K. Kim, N. H. Sung, J. D. Denlinger, and B. J. Kim, Observation of a d-wave gap in electron-doped SrIrO₄, *Nature Phys.* **12**, 37 (2016).
- [26] Y. J. Yan, M. Q. Ren, H. C. Xu, B. P. Xie, R. Tao, H. Y. Choi, N. Lee, Y. J. Choi, T. Zhang, and D. L. Feng, Electron-doped Sr₂IrO₄: An Analog of Hole-Doped Cuprate Superconductors Demonstrated by Scanning Tunneling Microscopy, *Phys. Rev. X* **5**, 041018 (2015).
- [27] K. Fujiwara, Y. Fukuma, J. Matsuno, H. Idzuchi, Y. Niimi, Y. Otani, and H. Takagi, 5d iridium oxide as a material for spin-current detection, *Nature Commun.* **4**, 2893 (2012).
- [28] M. Uchida, W. Sano, K. S. Takahashi, T. Koretsune, Y. Kozuka, R. Arita, Y. Tokura, and M. Kawasaki, Field-direction control of the type of charge carriers in nonsymmorphic IrO₂, *Phys. Rev. B* **91**, 241119 (2015).
- [29] X. Ming, K. Yamauchi, T. Oguchi, and S. Picozzi, Metal-insulator transition and $J_{\text{eff}} = 1/2$ spin-orbit insulating state in rutile-based IrO₂/TiO₂ superlattices, [arXiv:1702.04408](https://arxiv.org/abs/1702.04408).
- [30] F. G. Sen, A. Kinaci, B. Narayanan, S. K. Gray, M. J. Davis, S. K. R. S. Sankaranarayanan, and M. K. Y. Chan, Towards accurate prediction of catalytic activity in IrO₂ nanoclusters via first principles-based variable charge force field, *J. Mater. Chem. A* **3**, 18970 (2015).
- [31] C.-H. Lee, N. D. Orloff, T. Birol, Y. Zhu, V. Goian, E. Rocas, R. Haislmaier, E. Vlahos, J. A. Mundy, L. F. Kourkoutis, Y. Nie, M. D. Biegalski, J. Zhang, M. Bernhagen, N. A. Benedek, Y. Kim, J. D. Brock, R. Uecker, X. X. Xi, V. Gopalan, D. Nuzhnyy, S. Kamba, D. A. Muller, I. Takeuchi, J. C. Booth, C. J. Fennie, and D. G. Schlom, Exploiting dimensionality and defect mitigation to create tunable microwave dielectrics, *Nature (London)* **502**, 532 (2013).
- [32] S. Hikami, A. I. Larkin, and Y. Nagaoka, Spin-orbit interaction and magnetoresistance in the two dimensional random system, *Prog. Theor. Phys.* **63**, 707 (1980).
- [33] J. K. Kawasaki, C. H. Kim, J. N. Nelson, S. Crisp, C. J. Zollner, E. Biegenwald, J. T. Heron, C. J. Fennie, D. G. Schlom, and K. M. Shen, Engineering Carrier Effective Masses in Transition Metal Oxide Quantum Wells of IrO₂ (unpublished).
- [34] K. Yoshimatsu, K. Horiba, H. Kumigashira, T. Yoshida, A. Fujimori, and M. Oshima, Metallic quantum well states in artificial structures of strongly correlated oxide, *Science* **333**, 319 (2011).
- [35] W. D. Ryden, A. W. Lawson, and C. C. Sartain, Temperature dependence of the resistivity of RuO₂ and IrO₂, *Phys. Lett. A* **26**, 209 (1968).